

Optical Conductivity in a Two-Band Superconductor: Pb

N. Bock*

Theoretical Division, Los Alamos National Laboratory, Los Alamos, New Mexico 87545

D. Coffey

Dept. of Physics, Buffalo State College, Buffalo, New York 14222

(Dated: February 6, 2008)

We demonstrate the effect of bandstructure on the superconducting properties of Pb by calculating the strong-coupling features in the optical conductivity, $\sigma(\omega)$, due to the electron-phonon interaction. The importance of momentum dependence in the calculation of the properties of superconductors has previously been raised for MgB₂^{1,2}. Pb resembles MgB₂ in that it is a two band superconductor in which the bands' contributions to the Fermi surface have very different topologies. We calculate $\sigma(\omega)$ by calculating a memory function³ which has been recently used to analyze $\sigma(\omega)$ of Bi₂Sr₂CaCu₂O_{8+δ}⁴. In our calculations the two components of the Fermi surface are described by parameterizations of de Haas-van Alphen data. We use a phonon spectrum which is a fit to neutron scattering data. By including the momentum dependence of the Fermi surface good agreement is found with the experimentally determined strong-coupling features which can be described by a broad peak at around 4.5 meV and a narrower higher peak around 8 meV of equal height. The calculated features are found to be dominated by scattering between states within the third band. By contrast scattering between states in the second band leads to strong-coupling features in which the height of the high energy peak is reduced by $\sim 50\%$ compared to that of the low energy peak. This result is similar to that in the conventional isotropic (momentum independent) treatment of superconductivity. Our results show that it is important to use realistic models of the bandstructure and phonons, and to avoid using momentum averaged quantities, in calculations in order to get quantitatively accurate results. **LA-UR-06-4303**

PACS numbers: 74.25.Nf, 74.25.Gz, 74.25.Jb

I. INTRODUCTION

Suhl et al.⁵ originally introduced a two-band model for superconductors as an extension of the original BCS calculation in which each band has its own superconducting gap. This two-band model was proposed to explain fine structure in the infrared absorption of superconductors with *s* and *d* electrons. Many years later Allen⁶ proposed a formalism to extend the Eliashberg treatment of superconductivity to include multiband Fermi surfaces and Fermi surfaces with complicated geometry by expanding order parameters, pairing interactions and scattering mechanism in terms of Fermi surface harmonics. This formalism was employed by Golubov and Mazin⁷ to investigate the effect of impurity scattering on the value of the critical temperature in two-band model superconductors. Kresin and Wolf⁸ also discussed two band superconductivity in the context of the high T_c materials in which superconductivity in one band is induced in a second band by interband scattering. These investigations were not extended to get quantitative results for specific materials. Quantitative investigations of superconductivity in real multiband systems have only been developed in recent years with the availability of the necessary computational resources. Renewed interest in this area is driven by experiment. In 2001 Nagamatsu et al.⁹ discovered that MgB₂ becomes a superconductor at temperatures below $T_c = 39$ K. This value of T_c is comparable to that of La_{1-x}Sr_xCuO₄, the first of the cuprate superconductors to be discovered. This discovery initiated a number of theoretical and experimental studies on the nature of the superconducting state in this material. MgB₂ shows a significant isotope effect, a tell-tale sign of the involvement of phonons in the process¹⁰. Several tunneling experiments found very different values for the superconducting gap^{11,12}, which led Liu et al.¹³ to suggest that the superconducting state of MgB₂ exhibits multiple gaps. First principle calculations¹⁴ found essentially two distinct conduction bands, and it is this two-band nature of the MgB₂ system that is responsible for two different gaps. The calculated Fermi surface was subsequently found to be in agreement with angle resolved photoemission (ARPES)¹⁵ and de Haas-van Alphen¹⁶ measurements. Choi et al.^{1,2} calculated the gap function and T_c using the anisotropic Eliashberg formalism¹⁷ which incorporates the momentum dependence of the phonons, electronic bandstructure and the electron-phonon interaction. Choi et al. used the *ab initio* pseudopotential density-functional method to calculate these. They pointed to the strong variation in the electron-phonon interaction on and between the Fermi surfaces of the two bands in which the interband scattering is much weaker than intraband scattering because of the different symmetry of bands in MgB₂.^{1,2} The strong dependence of the electron-phonon coupling on Fermi surface states in MgB₂ leads to a wide range of values for the superconducting gap. Choi et al. emphasized the importance of including the momentum dependence of these quantities rather than using the

isotropic version of the Eliashberg equations for quantitatively accurate results. Here we show that there is also a strong dependence on bandstructure in the optical conductivity of superconducting lead. Pb is effectively a two band material in which the electron-phonon interband scattering is comparable to the intra-band scattering so that the superconducting gaps on the two bands are almost equal, in contrast to MgB₂. $T_c \sim 7.9$ K, is also much lower in Pb than in MgB₂. In order to investigate the importance of including the different character of the two bands which cross the Fermi level in Pb we calculate the strong-coupling features which appear in optical conductivity.

Optical conductivity can be thought of as having two contributions. The first one is associated with the anomalous skin effect, whereas the second is due to “bulk” properties of the metal. The anomalous skin effect depends on the nature of the scattering of electrons from the surface and arises from the breakdown of momentum conservation at the surface. This contribution was initially investigated theoretically by a number of authors in the normal state^{18,19,20}. In superconductors it was studied by Pippard using the phenomenological London model²⁰ and by Mattis and Bardeen on the basis of the BCS theory²¹. The second contribution, the “bulk” part, comes from scattering of the incident photons on phonons, impurities, or other forms of scattering centers, within a distance comparable to the skin depth from the surface. We will focus on the Holstein process, the simultaneous absorption and emission of phonons by an electron, and ignore impurity and electron-electron scattering in our calculations using a memory function approach. This has previously been investigated by Allen²².

Farnworth and Timusk^{23,24} studied the strong-coupling effects associated with the electron-phonon interaction by infrared absorption. They measured the frequency dependence of the light emitted from a cavity whose walls contain Pb. They analyzed their data by taking the derivative of the ratio of the signal from the cavity in the normal and the superconducting states which leads to a frequency dependence given by the difference of the derivatives of the absorptivity in the superconducting and normal states, $A_S(\omega)$ and $A_N(\omega)$. This procedure has the effect of subtracting out the anomalous skin effect contribution and of enhancing the difference between the normal and the superconducting states. This results in a transport version of the $\alpha^2 F$ function which arises in the Eliashberg formalism.

Farnworth and Timusk’s data, shown in Fig. 1, exhibits features associated with the phonon density of states at B, C, D, E, F, and G. In addition the data has a feature, A, at $\omega = 4\Delta_0$, where Δ_0 is the value of the superconducting gap. This feature could be thought of arising either from the phonon-mediated interaction between the superconducting quasi-particles or as an effect due to the change in the phonon self-energy in the superconducting state. The leading contribution to this feature is then fourth order in the strength of the electron-phonon coupling. The data of Farnworth and Timusk on thin films reveals a splitting of this feature into two slightly different but distinct energies indicating that we are dealing with two conduction bands in Pb²³.

We use the memory function formalism which was developed by Götze and Wölfle³ to calculate the contributions to $\sigma(\omega)$ due to scattering events from phonons, impurities, and spin fluctuations. The assumption of this approach is that the memory function, $M(\omega)$, can be expressed as a power series in the electron-phonon interaction strength, which makes this approach in principle a weak coupling approach. The advantage of this approach, compared to summing ladder diagrams, is that it is much easier to include the details of the Fermi surface which leads to improved quantitative agreement with experiment for Pb. Previously Tomlinson and Carbotte²⁵ have investigated the temperature dependence of the resistivity using the same experimental data as we use for Pb with different approximate solutions to the Boltzmann equation. Leung et al.²⁶ have also taken a similar approach for the resistivity of aluminum.

Recently Hwang et al.⁴ determined $M(\omega)$, referring to it as the “optical single-particle self-energy”, in their analysis of $\sigma(\omega)$ in Bi₂Sr₂CaCu₂O_{8+δ} and compared it with a single-particle self-energy derived from ARPES data. The interpretation of $\sigma(\omega)$ data in the high T_c materials, as well as other types of data, is considerably more difficult than in conventional electron-phonon superconductors. In high T_c superconductors strong correlation effects are evident in phenomena, such as the pseudogap, and are thought to be responsible for the high value of T_c . These correlation effects and the absence of a consensus on a suitable microscopic model make inversion of data and analysis based on weak coupling treatments problematic. Schachinger et al.²⁷ have recently investigated the inversion of $\sigma(\omega)$ data for conventional and high T_c superconductors using singular value decomposition and maximum entropy techniques.

In our calculations we use fits to the experimentally determined Fermi surface determined from de Haas-van Alphen data and phonons from neutron scattering data, rather than calculate these as Choi et al. did in the case of MgB₂. In Pb there are two 6s and two 6p electrons per atom leading to four bands. De Haas-van Alphen measurements and a subsequent analysis of these by Anderson and Gold²⁸ show that in Pb the lowest lying band is completely inside the Fermi surface, and that the second and third bands both cut across the Fermi energy, whereas the fourth band lies above the Fermi energy. The component of the Fermi surface due to the second band has the topology of a sphere while that due to the third band is multiply connected and has the form of cylinders along each edge of the first Brillouin zone. The two band nature of Pb is due to the second and third bands. The phonons are described by Cowley’s fit²⁹ to neutron scattering data.

In sections II and III we discuss our treatment of the charge carriers and the electron-phonon coupling. In section IV we derive an expression from the electron-phonon contribution to the memory function in the superconducting

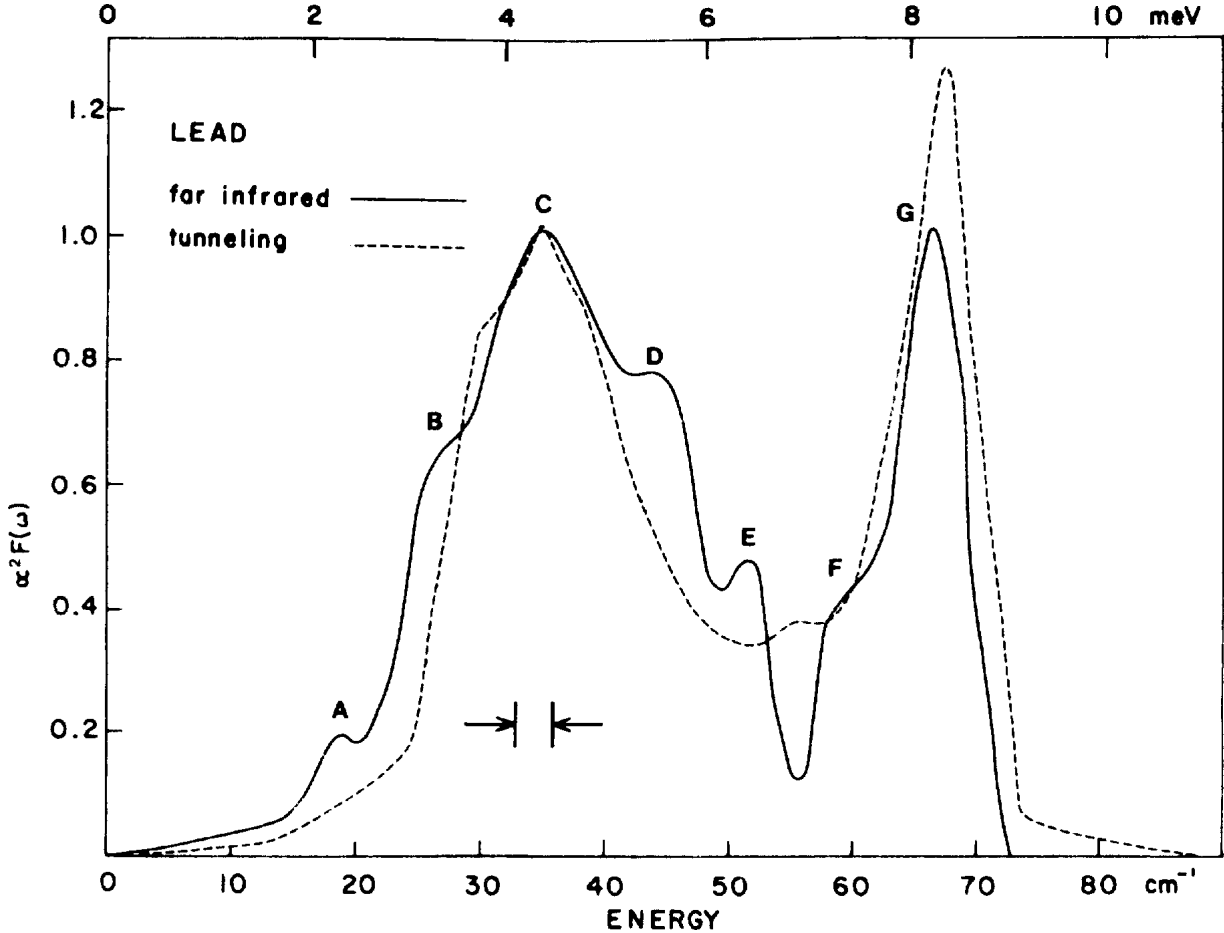


FIG. 1: Reproduced from reference 24 with permission: Comparison of $\alpha^2 F$ numerically inverted from infrared absorption (solid line) and tunneling (dashed line)

state and an expression for the absorptivity in terms of the memory function. After calculating the derivative of the difference of the calculated absorptivities in the normal and superconducting states we compare the result with the data of Farnworth and Timusk^{23, 24}. The comparison demonstrates the importance of scattering involving the third band and resolves the discrepancy between the experimentally determined $\alpha^2 F$ and that calculated ignoring momentum conservation and approximating the Fermi surface with a sphere²².

II. TWO-BAND CHARACTER

Anderson and Gold²⁸ carried out de Haas-van Alphen measurements on Pb and their subsequent analysis is based on the orthogonalized plane wave method which is fit to de Haas-van Alphen data of the Fermi surface. The Fermi energy, ϵ_F , the Fourier components of the pseudopotential parameters, V_{111} and V_{200} , and a spin-orbit coupling parameter λ are regarded as fitting parameters. We used the following values: $\epsilon_F = 9.765$ eV, $V_{111} = -1.142$ eV, $V_{200} = -0.530$ eV, and $\lambda = 1.306$ eV. Anderson and Gold's parameterization yields the dispersion relations for the 4 electron bands. The Fermi surface cuts through the second and third bands, which are shown in Figs. 2 and 3. Comparing these figures with the form of the Fermi surface calculated for an empty face center cubic lattice³⁰, one sees that the effect of interactions among the electrons is to remove the sharp edges in the second band and increase the density of electrons in the third band. Electron interactions also now ensure that the fourth band is empty at low temperatures whereas there is a small contribution to the electron density from the fourth band in the empty lattice calculation. By using this experimentally determined Fermi surface we have included the effects of electron-electron scattering in the dispersion of the second and third band carriers.

In order to capture the strong-coupling features, the contributions from scattering among the different components of the Fermi surface have to be evaluated very accurately. These contributions are given by six-dimensional integral and

require a large number of mesh points. The Anderson and Gold model requires the diagonalization of a complex valued matrix which becomes computationally prohibitive inside a numerical integration. Fortunately, superconductivity is effected by phonon exchange between electron states which are close to the Fermi energy and we can approximate the dispersion by a power series expansion about k_F at each point on the Fermi surface and retain only the linear term. This is because the maximum phonon energy is much less than the characteristic electronic energy scale and because there are no strong features in the density of states close to the Fermi energy. We therefore model the electronic dispersion in the second and third bands using a simpler relation,

$$\xi_{\vec{k}}^{(i)} = \hbar v_F^{(i)} \left| \left(\vec{k} - \vec{k}_F \right)_{\perp} \right|, \quad (1)$$

where $v_F^{(i)}$ is the Fermi velocity on band i as input and $\left| \left(\vec{k} - \vec{k}_F \right)_{\perp} \right|$ is the magnitude of the component of $\vec{k} - \vec{k}_F$ perpendicular to the Fermi surface at \vec{k} .

Using the Anderson and Gold matrix and averaging over the Fermi surface we find a value of $v_F^{(2)} = -1.367 \times 10^6 \text{ m s}^{-1} < 0$ and $v_F^{(3)} = 1.055 \times 10^6 \text{ m s}^{-1}$. The second band is hole-like and the third band electron-like. The location of the Fermi surface in k -space is somewhat complicated but we can make some simplifying assumptions. The second band is approximated well with a sphere and we use a constant k_F for $\xi_{\vec{k}}^{(2)}$. The third band is more complicated as shown in Fig. 3. The Fermi surface consists of “pipes” around the edges of the Brillouin zone. Details of the Fermi surface parameterization used in the calculations are given in the Appendix, section VII.

III. ELECTRON-PHONON MODEL

Use of the experimental data ensures that the important consequences of the electron-electron interactions at the low frequencies of interest here are included in the location of the Fermi surface and in the Fermi velocities for the second and third band carriers. As a result the Hamiltonian contains a pure band structure part, \mathcal{H}_{band} , and the electron-phonon Hamiltonian, \mathcal{H}_{el-ph} . The Hamiltonian is given by

$$\mathcal{H} = \mathcal{H}_{band} + \mathcal{H}_{el-ph} = \sum_{\vec{k} \nu=2,3 \sigma} \xi_{\vec{k}\nu} c_{\vec{k}\nu\sigma}^\dagger c_{\vec{k}\nu\sigma} + \sum_{\vec{k} \nu\nu' \sigma \vec{q}\vec{Q}\lambda} g_{\nu\nu'}(\vec{q}, \vec{Q}, \lambda) (a_{\vec{q}\lambda} + a_{\vec{q}\lambda}^\dagger) c_{\vec{k}+\vec{q}+\vec{Q}\nu\sigma}^\dagger c_{\vec{k}\nu'\sigma}. \quad (2)$$

In \mathcal{H}_{band} , the electron energies, $\xi_{\vec{k}\nu}$, are given by our parameterization of the Anderson and Gold model eq. (1), σ denotes the electron spin, ν denotes the electronic band. In \mathcal{H}_{el-ph} the $a_{\vec{q}\lambda}$ and $a_{\vec{q}\lambda}^\dagger$ are the usual creation and destruction operators for phonons and λ is the branch index for the phonon spectrum. The electron-phonon matrix element is

$$g_{(\nu\nu')}(\vec{q}, \vec{Q}, \lambda) = -i \sqrt{\frac{\hbar^2}{2N_0 M_{\text{Pb}} \hbar \omega_{\vec{q}\lambda}}} \hat{\eta}_{\vec{q}\lambda} \cdot (\vec{q} + \vec{Q}) V_{(\nu\nu')}(\vec{q} + \vec{Q}), \quad (3)$$

where the phonon spectrum, $\hbar \omega_{\vec{q}\lambda}$, and the phonon wavefunctions, $\hat{\eta}_{\vec{q}\lambda}$, are given by a force constant model for the phonon dispersion based on work done by Cowley²⁹. $V_{(\nu\nu')}(\vec{q})$ is the Fourier transform of the screened electron-ion pseudopotential describing scattering between the two electron bands in the problem. We modeled the three different electron-phonon matrix elements, $g_{(22)}(\vec{q}, \vec{Q}, \lambda)$, $g_{(23)}(\vec{q}, \vec{Q}, \lambda)$, $g_{(32)}(\vec{q}, \vec{Q}, \lambda)$ and $g_{(33)}(\vec{q}, \vec{Q}, \lambda)$, by a common pseudopotential function³¹ and scaling factors, so that $g_{(\nu\nu')}(\vec{q}, \vec{Q}, \lambda) = a_{(\nu\nu')} g(\vec{q}, \vec{Q}, \lambda)$. The values of the $a_{(\nu\nu')}$ are determined by fitting the solution of the gap equation to the experimentally determined values for the two bands²³, 1.29 meV and 1.38 meV, and are found to be $a_{(22)} = 0.61$, $a_{(23)} = 0.50$, and $a_{(33)} = 0.56$ ³².

IV. OPTICAL CONDUCTIVITY

The optical conductivity is given by

$$\sigma(\omega) = -i \left(\frac{e^2}{\omega} \right) \chi(\omega) + i \frac{\omega_{pl}^2}{4\pi\omega}, \quad (4)$$

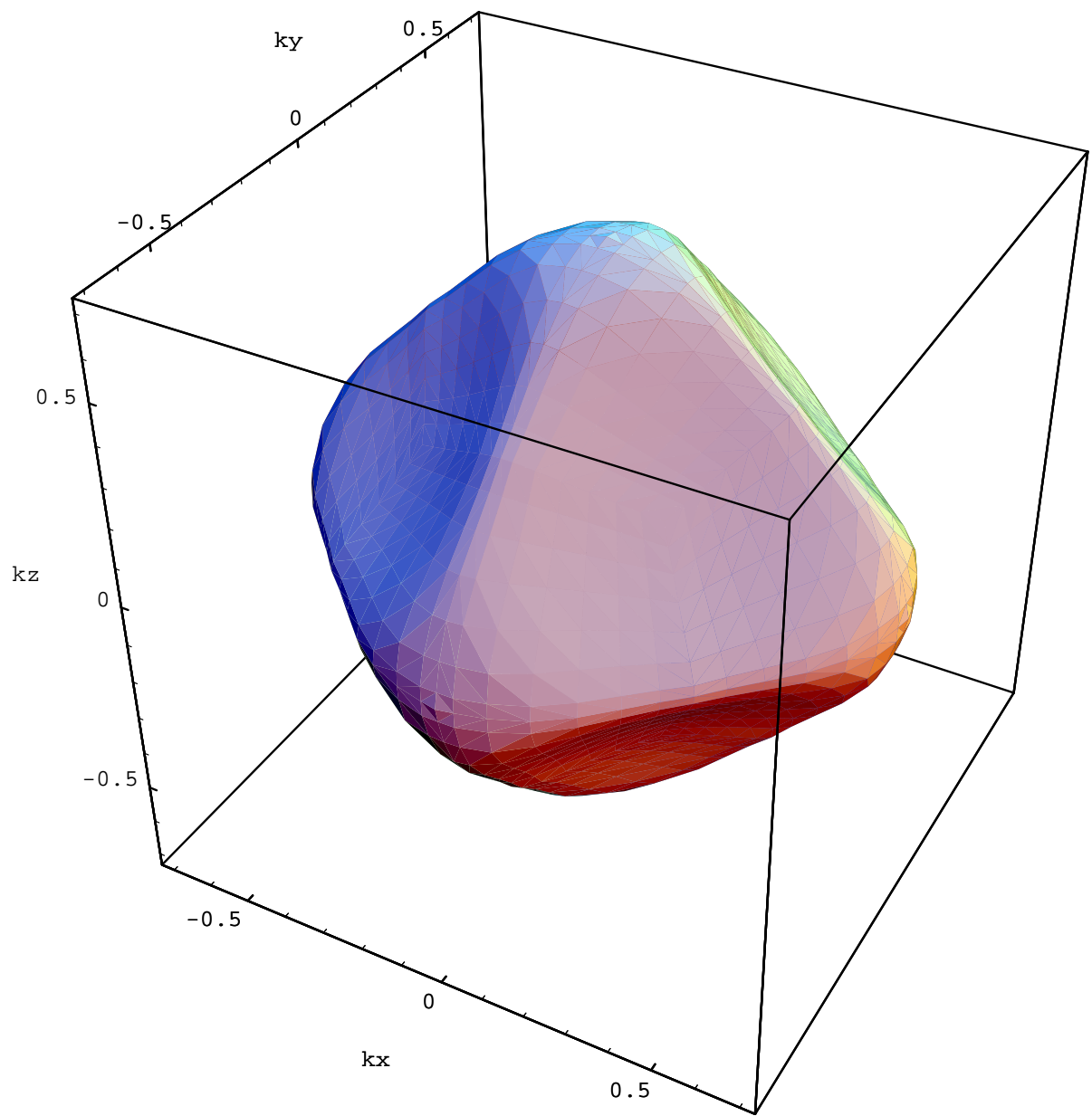


FIG. 2: (Color online) Second band in Pb calculated using the matrix by Anderson and Gold²⁸.

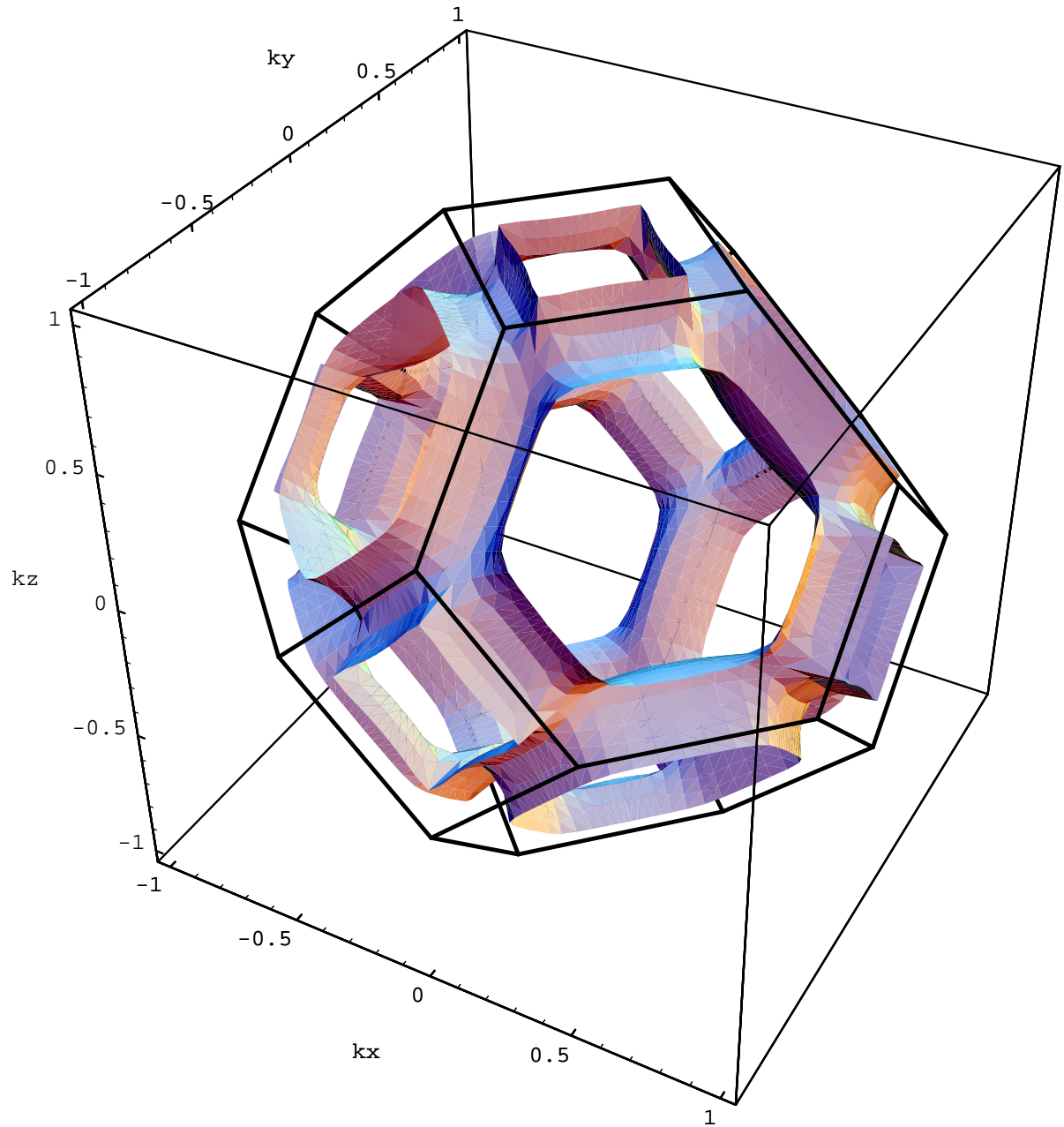


FIG. 3: (Color online) Third band in Pb calculated using the matrix by Anderson and Gold²⁸. The more complicated Fermi surface structure is illustrated by the “pipe” like tubes along the zone edges.

where $\chi(\omega) = \langle\langle j; j \rangle\rangle = -i \int_0^\infty dt \langle [j(t), j(0)] \rangle e^{i\omega t}$ is the retarded current-current correlation function. In the normal state the d.c. conductivity, $\sigma(0)$, is finite so that the poles in the two terms exactly cancel. Consequently $\chi(0) = \omega_{pl}^2 / (4\pi e^2) = n e^2 / m_{opt}^*$, where n is the density of carriers and m_{opt}^* is the optical effective mass. Götze and Wölfle reformulated this result in terms of a memory function, $M(\omega)$,

$$\sigma(\omega) = \frac{i}{4\pi} \frac{\omega_{pl}^2}{\omega + M(\omega)}, \quad (5)$$

where

$$M(\omega) = \frac{\omega\chi(\omega)}{\chi(0) - \chi(\omega)}. \quad (6)$$

In this formulation the cancellation of the poles at $\omega = 0$ is accomplished by introducing the memory function, $M(\omega)$, which remains to be determined. The analytic properties of the correlation functions require that the real part of $M(\omega)$, $M'(\omega)$, is odd in ω and that the imaginary part, $M''(\omega)$, is even. There are several potential contributions to $M(\omega)$ from different scattering mechanisms depending on the system being considered. Götze and Wölfle considered a number of mechanisms including impurity scattering and electron-phonon scattering, among others³.

A. Electron-Phonon Contribution

Here we are interested in the contribution from electron-phonon scattering which is characterized by the strength of the coupling, g . The functional form of $M(\omega)$ is found from $\chi(\omega)$ to second order in g by assuming that $M(\omega)$ is a power series in the strength of the electron-phonon interaction, g , so that, expanding the right hand side of eq. (6) one finds³

$$M(\omega) = \frac{[\langle\langle [j, H]; [j, H] \rangle\rangle_\omega - \langle\langle [j, H]; [j, H] \rangle\rangle_{\omega=0}]}{\omega\chi(0)} + O(g^4), \quad (7)$$

where

$$[j_i, H] = \sum_{\vec{k}, \nu, \vec{k}', \nu', \sigma} \left[\frac{\partial \xi_{\vec{k}, \sigma, \nu}}{\partial k_i} - \frac{\partial \xi_{\vec{k}', \sigma, \nu'}}{\partial k'_i} \right] c_{\vec{k}, \sigma, \nu}^\dagger c_{\vec{k}', \sigma, \nu'} (a_{\vec{k}-\vec{k}', \lambda}^\dagger + a_{-\vec{k}+\vec{k}', \lambda}), \quad (8)$$

and

$$j_i = \sum_{\vec{k}, \sigma, \nu} \frac{\partial \xi_{\vec{k}, \sigma, \nu}}{\partial k_i} c_{\vec{k}, \sigma, \nu}^\dagger c_{\vec{k}, \sigma, \nu}. \quad (9)$$

In the superconducting state the response of the supercurrent to the external field leads to a delta-function in $\sigma(\omega)$ at $\omega = 0$ in the real part and a pole in the imaginary part. The weight of the pole is given by $c^2 / (4\pi\lambda^2)$ (see Tinkham³³), where λ is the penetration depth. Using experimental values for Pb, $\chi(0)$ in the superconducting state is reduced from the normal state value by $\simeq 0.026$. This leads to a negligible quantitative effect for the frequencies of interest here, $\omega > 2\Delta$, and therefore we will ignore this.

In the following we drop the band index to simplify the notation. The correlation function in the superconducting state to lowest order in the strength of the electron-phonon interaction, $O(g^2)$, is

$$\langle\langle [j, H]; [j, H] \rangle\rangle_\omega = \langle\langle [j, H]; [j, H] \rangle\rangle_\omega^{(N)} + \langle\langle [j, H]; [j, H] \rangle\rangle_\omega^{(S)}, \quad (10)$$

where

$$\langle\langle [j, H]; [j, H] \rangle\rangle_\omega^{(N)} = \sum_{\vec{k}, \vec{q}, \lambda} \left[u_{\vec{k}}^2 u_{\vec{k}+\vec{q}}^2 + v_{\vec{k}}^2 v_{\vec{k}+\vec{q}}^2 - 2 u_{\vec{k}} v_{\vec{k}} u_{\vec{k}+\vec{q}} v_{\vec{k}+\vec{q}} \right] \left| \mathcal{M}(\vec{k}, \vec{q}, \lambda) \right|^2$$

$$\times \left[f_{\vec{k}+\vec{q}}(1-f_{\vec{k}})(1+n_{\vec{q}}) - f_{\vec{k}}(1-f_{\vec{k}+\vec{q}})n_{\vec{q}} \right] \left(\frac{1}{E_{\vec{k}} + \omega_{\vec{q}} - E_{\vec{k}+\vec{q}} - \omega} + \frac{1}{E_{\vec{k}} + \omega_{\vec{q}} - E_{\vec{k}+\vec{q}} + \omega} \right)$$

and

$$\begin{aligned} \langle\langle [j, H]; [j, H] \rangle\rangle_{\omega}^{(S)} &= \sum_{\vec{k}, \vec{q}, \lambda} \left[u_{\vec{k}}^2 v_{\vec{k}+\vec{q}}^2 + v_{\vec{k}}^2 u_{\vec{k}+\vec{q}}^2 + 2u_{\vec{k}} v_{\vec{k}} u_{\vec{k}+\vec{q}} v_{\vec{k}+\vec{q}} \right] |\mathcal{M}(\vec{k}, \vec{q}, \lambda)|^2 \\ &\times \left[(1-f_{\vec{k}+\vec{q}})(1-f_{\vec{k}}) \left(\frac{2(\omega_{\vec{q}} + E_{\vec{k}+\vec{q}} + E_{\vec{k}})(1+n_{\vec{q}})}{(\omega_{\vec{q}} + E_{\vec{k}+\vec{q}} + E_{\vec{k}})^2 - \omega^2} + \frac{2(\omega_{\vec{q}} - E_{\vec{k}+\vec{q}} - E_{\vec{k}})n_{\vec{q}}}{(\omega_{\vec{q}} - E_{\vec{k}+\vec{q}} - E_{\vec{k}})^2 - \omega^2} \right) \right. \\ &\left. - f_{\vec{k}} f_{\vec{k}+\vec{q}} \left(\frac{2(\omega_{\vec{q}} - E_{\vec{k}+\vec{q}} - E_{\vec{k}})(1+n_{\vec{q}})}{(\omega_{\vec{q}} - E_{\vec{k}+\vec{q}} - E_{\vec{k}})^2 - \omega^2} + \frac{2(\omega_{\vec{q}} + E_{\vec{k}+\vec{q}} + E_{\vec{k}})n_{\vec{q}}}{(\omega_{\vec{q}} + E_{\vec{k}+\vec{q}} + E_{\vec{k}})^2 - \omega^2} \right) \right]. \end{aligned}$$

The $u_{\vec{k}}$ and $v_{\vec{k}}$ are the usual BCS coherence factors. $\mathcal{M}(\vec{k}, \vec{q}, \lambda)$ is the electron-phonon interaction defined earlier together with the derivatives of the quasiparticle spectrum in the current operator,

$$\mathcal{M}(\vec{k}, \vec{q}, \lambda) = -i \sqrt{\frac{N_0 \hbar^2}{2M_{\text{Pb}} \hbar \omega_{\vec{k}-\vec{k}'}^{\lambda}}} [\vec{k} - \vec{k}' \cdot \eta_{\vec{k}-\vec{k}'}^{\lambda}] V_{(\nu\nu')}(\vec{k} - \vec{k}') \left[\frac{\partial \xi_{\vec{k}, \sigma, \nu}}{\partial k_i} - \frac{\partial \xi_{\vec{k}', \sigma, \nu'}}{\partial k'_i} \right] \quad (11)$$

$\langle\langle [j, H]; [j, H] \rangle\rangle_{\omega}^{(N)}$ has the character of a particle-hole contribution and smoothly evolves into the normal state result derived by Allen²² and by Götze and Wölfle³. It is exponentially small for temperatures much smaller than the gap and is negligible at the temperature at which Farnworth and Timusk took their data on lead in the superconducting phase, 0.35 K. On the other hand the combination of coherence factors and the particle-particle or hole-hole distribution functions ensures that $\langle\langle [j, H]; [j, H] \rangle\rangle_{\omega}^{(S)}$ vanishes as the gap vanishes. This term gives the conductivity at finite frequencies at low temperatures much less than T_c . Taking the limit as $T \rightarrow 0$, the real and imaginary parts of $M_S(\omega)$ become

$$\begin{aligned} M^{S'}(\omega) &= \sum_{\vec{k}, \vec{q}} \left[u_{\vec{k}}^2 v_{\vec{k}+\vec{q}}^2 + v_{\vec{k}}^2 u_{\vec{k}+\vec{q}}^2 + 2u_{\vec{k}} v_{\vec{k}} u_{\vec{k}+\vec{q}} v_{\vec{k}+\vec{q}} \right] \frac{|\mathcal{M}(\vec{k}, \vec{q}, \lambda)|^2}{\chi(0)} \\ &\times \frac{2\omega}{[(\omega_{\vec{q}} + E_{\vec{k}+\vec{q}} + E_{\vec{k}})^2 - \omega^2][\omega_{\vec{q}} + E_{\vec{k}+\vec{q}} + E_{\vec{k}}]} \\ M^{S''}(\omega) &= \pi \sum_{\vec{k}, \vec{q}} \left[u_{\vec{k}}^2 v_{\vec{k}+\vec{q}}^2 + v_{\vec{k}}^2 u_{\vec{k}+\vec{q}}^2 + 2u_{\vec{k}} v_{\vec{k}} u_{\vec{k}+\vec{q}} v_{\vec{k}+\vec{q}} \right] \frac{|\mathcal{M}(\vec{k}, \vec{q}, \lambda)|^2}{\chi(0)} \\ &\times \left(\frac{\delta[\omega - (\omega_{\vec{q}} + E_{\vec{k}+\vec{q}} + E_{\vec{k}})] + \delta[\omega + (\omega_{\vec{q}} + E_{\vec{k}+\vec{q}} + E_{\vec{k}})]}{\omega_{\vec{q}} + E_{\vec{k}+\vec{q}} + E_{\vec{k}}} \right) \quad (12) \end{aligned}$$

B. Absorptivity

The absorptivity is proportional to the real part of the surface impedance, $(1 + (4\pi i/\omega)\sigma(\omega))^{-1/2}$. As a minimal model we ignore the difference between the values of the gaps on the Fermi surfaces associated with the second and third bands and take $\Delta_0 = 1.37$ meV. This is an average of the two values found by Farnworth and Timusk²³. We will therefore get three contributions to the memory function, $M(\omega)$, and to the absorptivity. These three are from intra-band scattering within the second band, $M_{(22)}(\omega)$, intra-band scattering within the third band, $M_{(33)}(\omega)$, and inter-band scattering between the second and the third band, $M_{(23)}(\omega)$. Since the frequencies of interest are much smaller than the plasma frequency, ω_{pl} , the expression for the absorptivity $A(\omega)$ can be greatly simplified.

$$A(\omega) \simeq \frac{4\omega}{\omega_{pl}} \sqrt{2 \left(\left| 1 + \frac{M(\omega)}{\omega} \right| - \left[1 + \frac{M'(\omega)}{\omega} \right] \right)} \simeq \frac{2}{\omega_{pl}} \frac{M''(\omega)}{\sqrt{1 + \frac{M'(\omega)}{\omega}}} \quad (13)$$

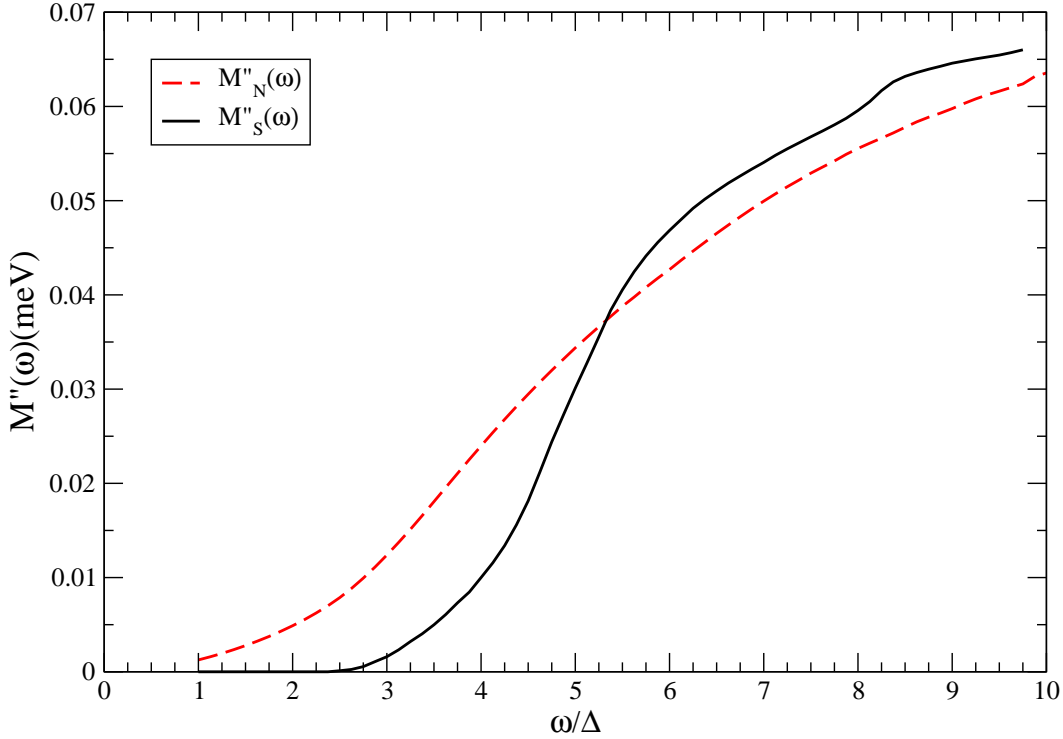


FIG. 4: (Color Online) $M''_{(22)}(\omega)$ vs. ω . The full line is $M''_{(22)}^S(\omega)$ in the superconducting state while the dashed line is $M''_{(22)}^N(\omega)$ in the normal state.

Here we have also assumed that $1 + \frac{M'(\omega)}{\omega} > 1$ and $\frac{M''(\omega)}{\omega} < 1$ so that square root can be expanded. $\frac{M'(\omega)}{\omega}$ evaluated at $\omega = 0$ is the enhancement of the optical effective mass which is similar to the enhancement of the effective mass due to the electron-phonon interaction in the specific heat.

The $M''_{(22)}$, $M''_{(23)}(\omega)$, and $M''_{(33)}(\omega)$ contributions in the normal and superconducting states to order g^2 are compared in Figs. 4, 5, and 6. The different magnitudes of the memory functions $M_{(ij)}(\omega)$, reflects their dependence on the surface area of the different parts of the Fermi surface involved in the scattering processes and on the size of the phase space for phonons which connect different parts of the Fermi surface. This dominates any effects the density of states on the different Fermi surfaces might have due to the cancellation of the Fermi velocity factors in the density of states with those from the current operator matrix elements.

The dominant contribution comes from $M''_{(33)}(\omega)$ which involves the scattering between the 36 “pipes” which make up the third band. Although the geometry of the third band suggests that quasi-one dimensional “nesting”, scattering between parallel pipes with a single phonon momentum, could be important, it is found not to dominate $M''_{(33)}(\omega)$.

There are $\frac{36^2}{2} = 648$ different combinations of pipes and of those, pipes whose mid-points can be connected by momentum vectors $\vec{Q}_1 = 2\pi/a(1, 1/2, 1/2)$ and $\vec{Q}_2 = 2\pi/a(3/2, 0, 0)$ lead to contributions much larger than other combinations by about a factor of ~ 10 . There are only approximately 100 of these combinations and their contribution does not dominate $M''_{(33)}(\omega)$.

In contrast to the intra-band scattering events on the second band, there are many more phonons that connect the more complicated surface of the third band. This and the larger surface area of the third zone Fermi surface is responsible for the big difference in magnitude of the two contributions.

The real parts of the $M_{(ij)}$ are related to the imaginary parts through a Kramers-Kronig relation, $M'(\omega) = \frac{2\omega}{\pi} \int_0^\infty dz \frac{M''(z)}{z^2 - \omega^2}$, so that $M'(\omega)$ can, in principle, be calculated directly from $M''(\omega)$. Consequently the magnitudes of

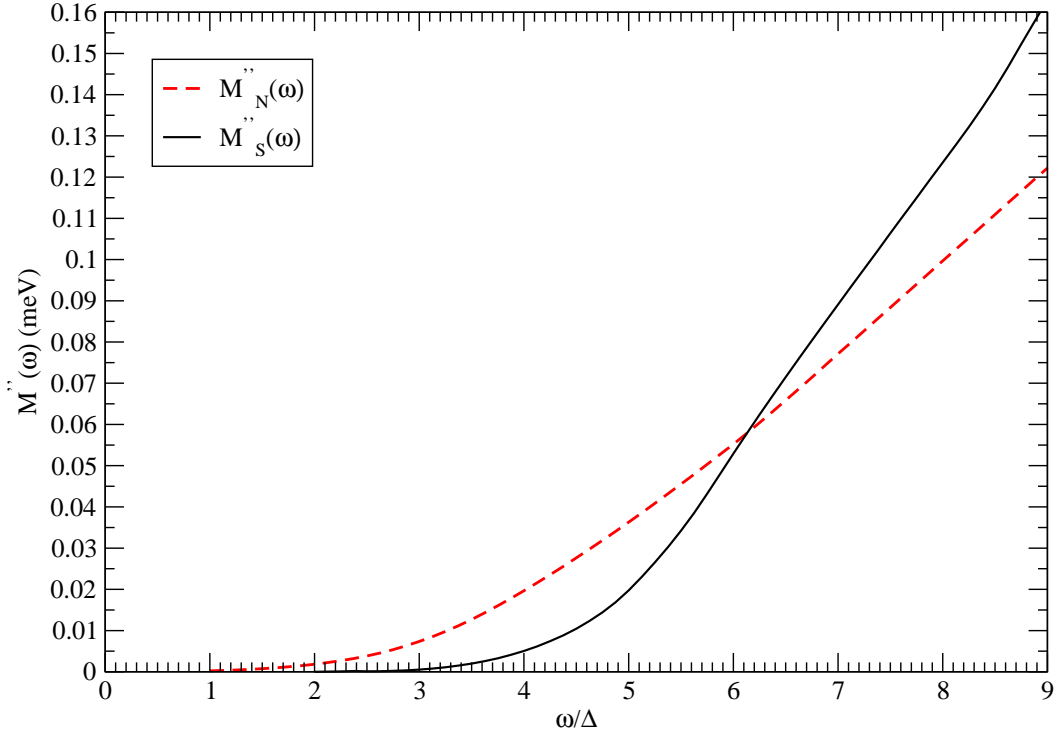


FIG. 5: (Color Online) $M''_{(23)}(\omega)$ vs. ω . The full line is $M''_{(23)}(\omega)$ in the superconducting state while the dashed line is $M''_{(23)}(\omega)$ in the normal state.

the real parts of the $M_{(ij)}$ have a similar relation to one another as the imaginary parts. $\lim_{\omega \rightarrow 0} M'(\omega)/\omega$ corresponds to the optical effective mass enhancement due to the electron–phonon interaction, similar to the enhancement seen in the specific heat. $M'(\omega)/\omega$ in the superconducting and normal states are smooth functions of ω which initially increase from their $\omega = 0$ values and reach maximum values at approximately 3Δ in the normal state and approximately 5Δ in the superconducting state before falling off monotonically with increasing ω . Beyond $\omega = 6\Delta$ they are almost equal in magnitude.

C. Strong-Coupling Features

In order to analyze the results further, we follow Farnsworth and Timusk and take the derivative of $A(\omega)$ with respect to ω . This reveals the strong-coupling electron–phonon features.

$$\frac{dA_S(\omega)}{d\omega} - \frac{dA_N(\omega)}{d\omega} \propto \frac{dM^{S''}(\omega)}{d\omega} - \frac{dM^{N''}(\omega)}{d\omega} \quad (14)$$

The strong-coupling features come almost exclusively from the first term on the right-hand side of the equation. In figures 7, 8, 9, and 10 we compare the contributions from the different scattering processes to $dM^{S''}(\omega)/d\omega$. In each case the peaks at $\simeq 35 \text{ cm}^{-1}$ and $\simeq 70 \text{ cm}^{-1}$, present in the data of Farnsworth and Timusk, are recovered. These peaks come from features in the phonon density of states and are associated with a wide range of wavenumbers. The $M^{N''}(\omega)$ in the normal state is featureless above 4Δ and subtracting from the superconducting $M^{S''}(\omega)$ does not introduce features not already present.

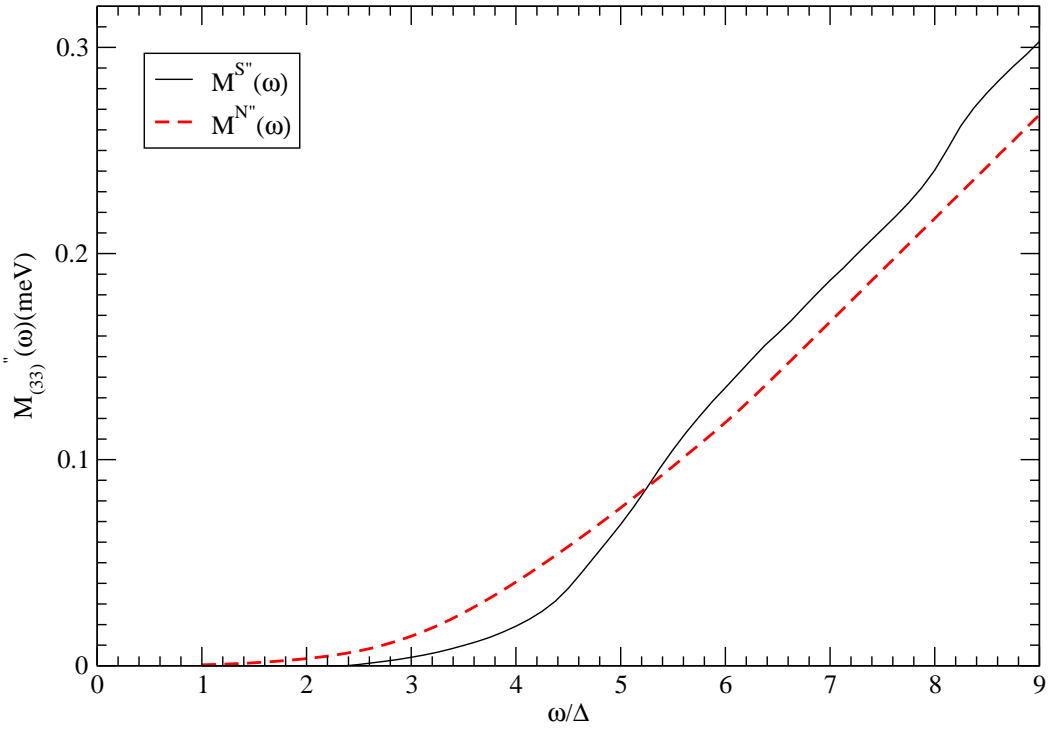


FIG. 6: (Color Online) $M''_{(33)}(\omega)$ vs. ω . The dashed line is $M''_{(33)}(\omega)$ in the superconducting state while the full line is $M''_{(33)}(\omega)$ in the normal state.

$M''_{(33)}(\omega)$ is the dominant contribution to $M''(\omega)$ and its derivative strongly resembles the data in Farnworth and Timusk²⁴. The two prominent peaks at C and G closely resemble the peaks at the same energies in Fig. 9 from the point of view of both height and width. The features at B, D and E are also seen in Fig. 9 and the relative magnitude of the calculated $dM''/d\omega$ at E and at C and G is the same as in the data. The interband scattering contribution, $dM''_{(23)}/d\omega$, enhances equally the magnitudes of the peaks at C and G but shows none of the other features. These differences arise from the shape of the two contributions to the Fermi surface from the two bands. Scattering between different parts of the third band Fermi surface introduces all the phonon modes and as a result it is the dominant contribution and closely resembles the phonon density of states. By contrast scattering within the second band constrains the phase space for phonons which conserve energy and momentum. The magnitude of the higher energy peak in $dM''_{(22)}(\omega)/d\omega$ is much smaller than that of the low energy peak, whereas the peaks are of equal magnitude in $dM''_{(23)}(\omega)/d\omega$ and $dM''_{(33)}(\omega)/d\omega$. The high energy peak comes from phonons whose energy is ~ 8.48 meV. In the case of $M_{22}(\omega)$ the magnitude of the wavenumbers of the phonons with this energy lie between 1.33 \AA^{-1} and 1.43 \AA^{-1} . By contrast the corresponding phonon wavenumbers in the case of $M_{33}(\omega)$ are grouped in sets with $|\vec{q}| \sim 0.78 \text{ \AA}^{-1}$, $\sim 0.8 \text{ \AA}^{-1}$, $\sim 0.86 \text{ \AA}^{-1}$, and $\sim 0.88 \text{ \AA}^{-1}$. In Fig. 10 we show the different contributions to $dM''/d\omega$.

In Fig. 11 we plot the calculated difference of the derivatives of $A_S(\omega)$ and $A_N(\omega)$ frequency shifted downwards by 2Δ for direct comparison with Farnworth and Timusk's data. We have also shifted Farnworth and Timusk's data by 0.9 cm^{-1} which takes account of the slightly different values of Δ used by them and us. Many of the features of the experimental data are reproduced: the shoulder B ($\sim 27 \text{ cm}^{-1}$) is enhanced in our calculation, the peaks at C ($\sim 36 \text{ cm}^{-1}$) and at G ($\sim 67 \text{ cm}^{-1}$) are recovered and are equal in magnitude as in the data, and the small feature at E ($\sim 52 \text{ cm}^{-1}$) is reproduced. The shoulder at D ($\sim 50 \text{ cm}^{-1}$) is much weaker in the calculation compared to the data and the dip at $\sim 56 \text{ cm}^{-1}$ between E and F is missing. These discrepancies in the $dM''/d\omega$ are probably due

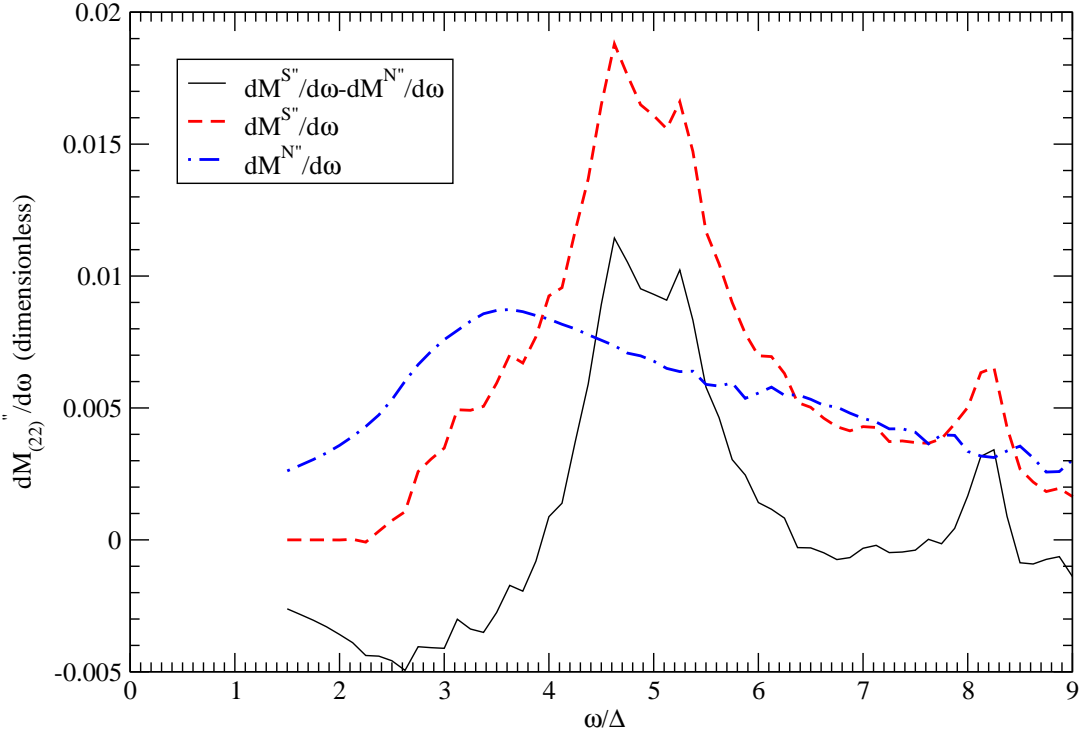


FIG. 7: (Color Online) The difference between $d''M_{(22)}(\omega)/d\omega$ (full line) in the superconducting and normal states.

to our parameterization of the Fermi surface. As we pointed out earlier, the feature at A arises from contributions which are fourth order in the electron-phonon coupling and so are naturally absent from our calculation.

The contribution to $\sigma(\omega)$ from the Holstein process in Pb was investigated many years ago by Allen²². He used the isotropic approximation familiar from the conventional Eliashberg formalism in which momentum conservation is not enforced in the electron-phonon scattering. In this approach the details of the bandstructure are completely absent. He introduced a transport version of the $\alpha^2 F(\omega)$, $\alpha_{tr}^2 F(\omega)$, in which the high frequency components were reduced to allow for the suppression of forward scattering in the matrix element. He used this to evaluated a frequency dependent relaxation time. This amounts to putting in by hand the strong-coupling features which we have calculated by taking the derivatives of the $M''_{ij}(\omega)$'s. Allen used the isotropic approximation to calculate this contribution to $\sigma(\omega)$. His result, $\alpha_{tr}^2 F(\omega)$ (Fig. 4 of Allen²²), is very similar to $dM''_{22}(\omega)/d\omega$ in Fig. 7. The main features at 4–5 meV and at ~ 8 meV are recovered. However, as he remarked, there is a discrepancy between the calculation of the absorptivity and the data of Joyce and Richards³⁴ and he offered a number of possible sources for this. Our calculation indicates that this discrepancy arises from the use of the isotropic approximation for the Fermi surface.

Allen suggested that one source of the discrepancy between his calculation and the data could be the absence of strong coupling corrections described by a frequency dependent gap function as calculated from the Eliashberg equations. Our calculation, using a momentum and frequency independent gap, reproduces much of the fine structure seen in the strong-coupling features and it seems likely that the differences with the data may be due to simplifications in the parameterization of the Fermi surface or phonon spectrum. However the absence of structure in the gap function could lead to corrections. Allen referred to a formalism for including a gap with structure developed by Nam³⁵ which incorporates details of the scattering mechanism by using the single-particle self-energy determined by the Eliashberg equations. Apart from the lack of momentum conservation in this conventional application of these equations, which could be fixed by adding momentum dependence^{1,2}, the single-particle lifetime is not the same as the transport relaxation time which is given by $M''(\omega)$ in our calculation. A more complete theory remains to be developed which

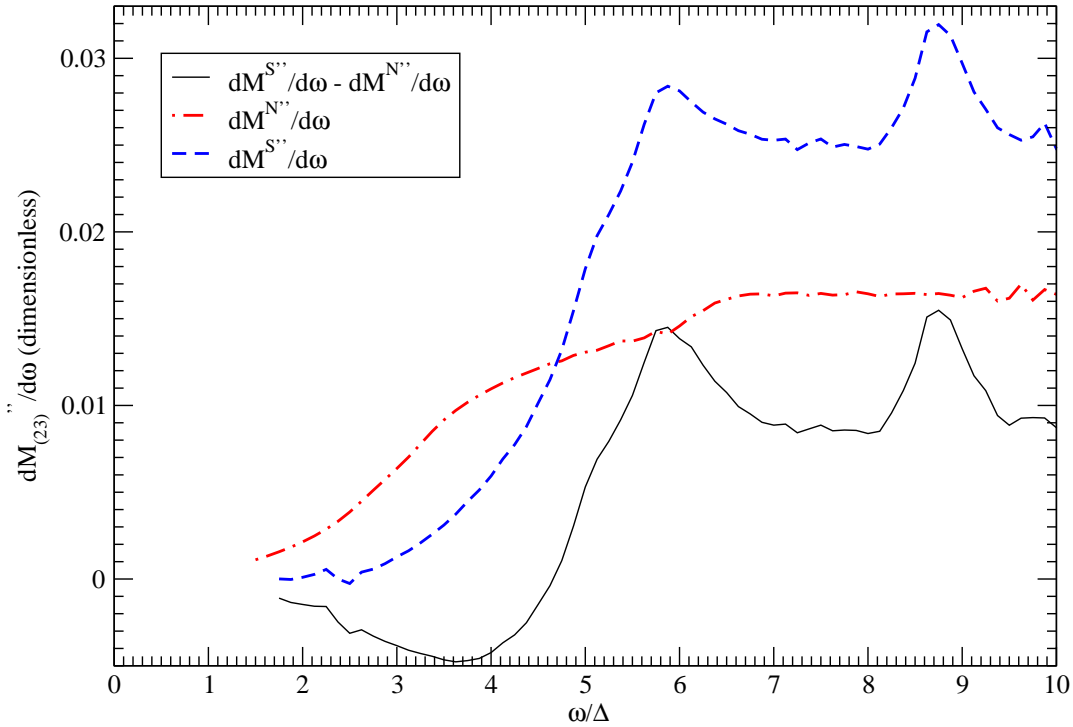


FIG. 8: (Color Online) The difference between $d''M_{(23)}(\omega)/d\omega$ (full line) in the superconducting and normal states.

incorporates both a realistic Fermi surface and corrections to the constant gap approximation.

Finally, we comment on the identification of $M(\omega)$, an “optical single-particle self-energy”, with the single-particle self-energy, as extracted from ARPES by Hwang et al.⁴ in their analysis of data on $\text{Bi}_2\text{Sr}_2\text{CaCu}_2\text{O}_{8+\delta}$. In the electron-phonon model discussed here the $M''_{(ij)}(\omega)$ ’s are quite different in form from the well-known imaginary part of the single-particle self-energy due to the electron-phonon interaction, $\Sigma''(E)$, as shown in Figure 6.16 of Mahan³⁶. Although $\Sigma(E)$ and the $M(\omega)$ have the same analytic requirements, the real parts are odd in frequency while imaginary parts are even, so that they have similar behavior at low frequencies, their finite frequency behavior is quite different. The imaginary part of the self-energy is constant beyond ~ 10 meV or $\sim 7.3\Delta_0$ whereas $M''_{(ij)}(\omega)$ ’s grow monotonically as the phase space for quasiparticle states increases with ω . Further, in the superconducting state, a feature associated with a peak in the phonon density of states, which appears at ω_{ph} (say), appears at $\Delta + \omega_{ph}$ in $\Sigma''(E)$ but at $2\Delta + \omega_{ph}$ in $M''(\omega)$. If further analysis of data on $\text{Bi}_2\text{Sr}_2\text{CaCu}_2\text{O}_{8+\delta}$ continues to support the proposed relation between $M(\omega)$ and $\Sigma(E)$, this will provide a strong constraint on the underlying Hamiltonian.

V. CONCLUSIONS

Using the memory function formalism we have demonstrated the importance of including a realistic Fermi surface in Pb to obtain quantitative agreement with the strong-coupling features seen in the optical data. The largest contribution to the strong-coupling features comes from intra-third band scattering which also provides most of the fine structure. The phonons involved in scattering within this band are not as restricted by momentum conservation as those involved in intra-second band scattering because the third band contribution to the Fermi surface is spread over a substantial fraction of the region near the zone boundary. This seems to be the reason why the $\alpha^2 F(\omega)$ determined from tunneling and that determined from $\sigma(\omega)$ are very similar, whereas one might have assumed that suppression of

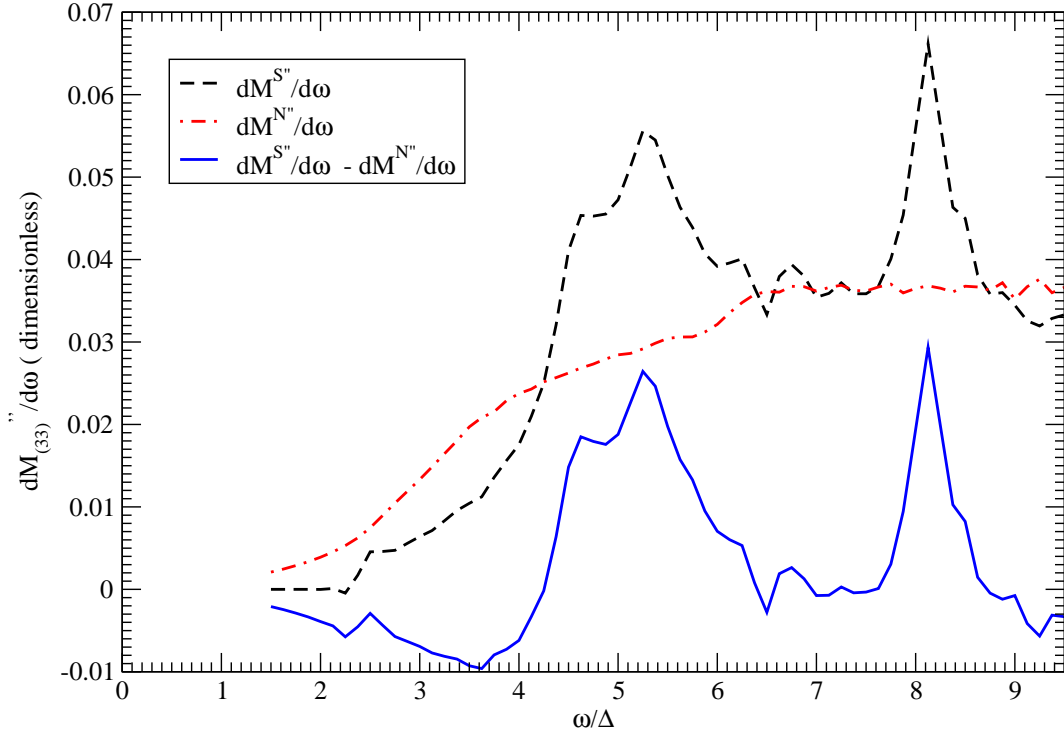


FIG. 9: (Color Online) The difference between $d''M_{(33)}(\omega)/d\omega$ (full line) in the superconducting and normal states. Note that the peak at ~ 8.5 meV has the same height as that at 5.5 meV. This reproduces an important feature of the Farnworth and Timusk data²⁴.

forward scattering in the current matrix elements would have lead to a difference between them. Allen's investigation of the relation between $\alpha^2 F(\omega)$ and $\alpha_{tr}^2 F(\omega)$ assumed a spherical Fermi surface and his model for $\alpha_{tr}^2 F(\omega)$ is very similar to the strong coupling features found from scattering between states on a spherical Fermi surface, $dM''_{(22)}/d\omega$ above.

Strong-coupling features in tunneling and transport data are a useful check on microscopic models of the mechanism for superconductivity. There are a number of systems in which mechanisms other than the electron-phonon interaction are thought to play a role. Among these are the cuprates where the contribution of the electron-phonon interaction remains to be clarified and in which the magnetic properties have been proposed as the origin of the d-wave superconductivity. Analysis of data so far finds no evidence of electron-phonon strong coupling features³⁷, although Maksimov et al.³⁸ have proposed a model for the electron-phonon interaction with which they have analyzed ARPES data on $\text{Bi}_2\text{Sr}_2\text{CaCu}_2\text{O}_8$. The data of Hwang et al.⁴ show that $M''(\omega)$ for $\text{Bi}_2\text{Sr}_2\text{CaCu}_2\text{O}_{8+\delta}$ has the same monotonic frequency dependence as was found in current work on Pb at low temperatures so that its derivative may reveal strong-coupling features associated with a magnetic mechanism. Analysis of data on the cuprates to date has employed the same formalism as in the electron-phonon problem with the $\alpha_{tr}F(\omega)$ function replaced with a spectral density for spin fluctuations. The weak coupling approximation introduced by Götze and Wölfle³ would have to be extended to calculate the contributions to $M(\omega)$ from electron-phonon or impurity scattering enhanced by spin fluctuations or from Umklapp scattering due to interactions among the charge carriers. Riseborough³⁹ has previously calculated the contribution from Umklapp scattering due to spin fluctuations in the random phase approximation using the Kubo formalism. A memory function approach extended to deal with intermediate to strong coupling could provide a method to test microscopic models for spin fluctuation mechanisms for superconductivity in the cuprates while taking account of bandstructure and momentum conservation.

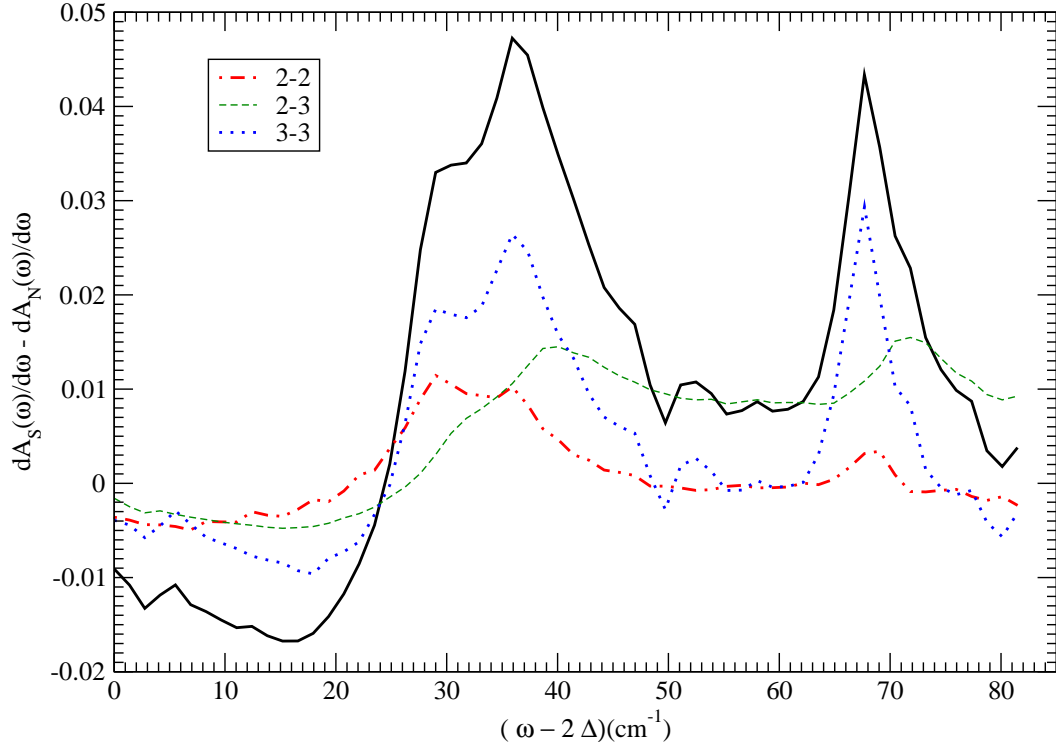


FIG. 10: (Color Online) Contributions to $dA_S(\omega)/d\omega - dA_N(\omega)/d\omega$ plotted against $\omega - 2\Delta$ in units of cm^{-1} (full line) from the three types of scattering processes.

VI. ACKNOWLEDGMENTS

We acknowledge P. Waltner for technical assistance with the representation of the Fermi surface and D. C. is grateful to L. Coffey for useful discussions. D. C. was supported in part by USDOE (DE-FG02-03ER46064).

* Electronic address: nbock@lanl.gov

- ¹ H. J. Choi, D. Roundy, H. Sun, M. L. Cohen, and S. G. Louie, Phys. Rev. B **66**, 020513(R) (2002).
- ² H. J. Choi, D. Roundy, H. Sun, M. L. Cohen, and S. G. Louie, Nature **418**, 758 (2002).
- ³ W. Götze and P. Wölfle, Phys. Rev. B **6**, 1226 (1972).
- ⁴ J. Hwang, T. Timusk, and G. D. Gu, Nature **427**, 714 (2004).
- ⁵ H. Suhl, B. T. Matthias, and L. R. Walker, Phys. Rev. Lett. **3**, 552 (1959).
- ⁶ P. B. Allen, Phys. Rev. B **13**, 1416 (1976).
- ⁷ A. A. Golubov and I. I. Mazin, Phys. Rev. B **55**, 15146 (1997).
- ⁸ V. Z. Kresin and S. A. Wolf, Phys. Rev. B **46**, 6458 (1992).
- ⁹ J. Nagamatsu, N. Nakagawa, T. Muranaka, Z. Y., and J. Akimitsu, Nature **410**, 63 (2001).
- ¹⁰ S. L. Bud'ko, G. Lapertot, C. Petrovic, C. E. Cunningham, N. Anderson, and P. C. Canfield, Phys. Rev. Lett. **86**, 1877 (2001).
- ¹¹ G. Rubio-Bollinger, H. Suderow, and S. Vieira, Phys. Rev. Lett. **86**, 5582 (2001).
- ¹² H. Schmidt, J. F. Zasadzinski, K. E. Gray, and D. G. Hinks, Phys. Rev. B **63**, 220504(R) (2001).
- ¹³ A. Y. Liu, I. I. Mazin, and J. Kortus, Phys. Rev. Lett. **87**, 087005 (2001).
- ¹⁴ J. Kortus, I. I. Mazin, K. D. Belashchenko, V. P. Antropov, and L. L. Boyer, Phys. Rev. Lett. **86**, 4656 (2001).

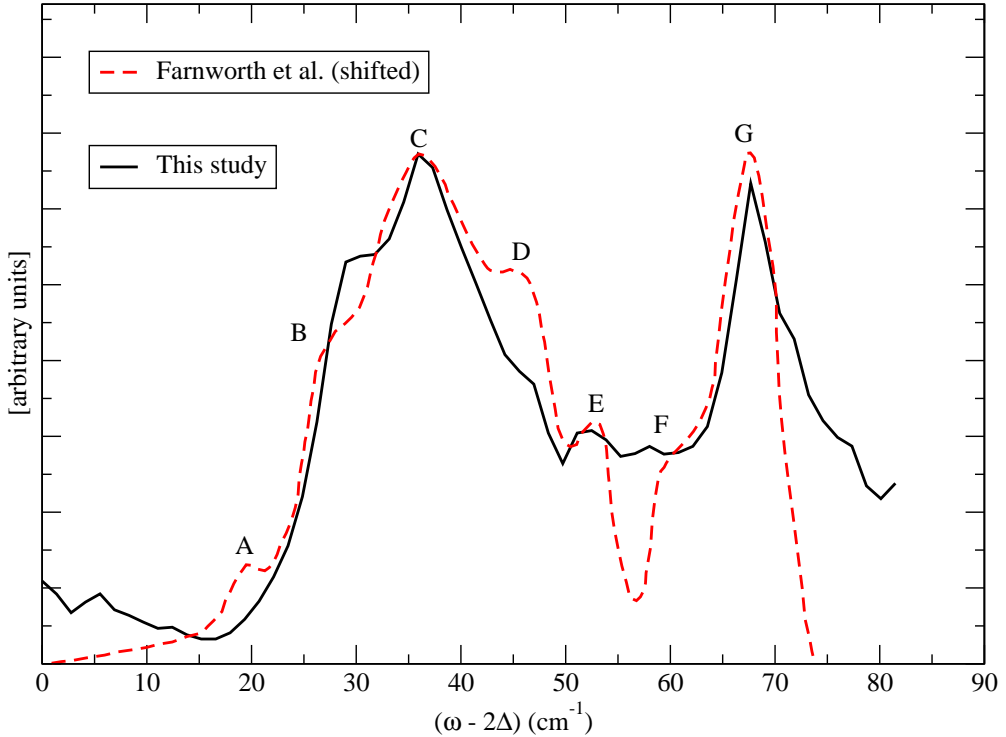


FIG. 11: (Color Online) $dA_S(\omega)/d\omega - dA_N(\omega)/d\omega$ plotted against $\omega - 2\Delta$ in units of cm^{-1} (full line). Many of the features of Farnworth and Timusk's data, shown in Fig. 1 are reproduced. Note that the peak G at ~ 8.5 meV has the same height as the peak C at 5.5 meV. This reproduces the most prominent feature of the Farnworth and Timusk data²⁴.

- ¹⁵ H. Uchiyama, K. M. Shen, S. Lee, A. Damascelli, D. H. Lu, D. L. Feng, Z.-X. Shen, and S. Tajima, Phys. Rev. Lett. **88**, 157002 (2002).
- ¹⁶ A. Carrington, P. J. Meeson, J. R. Cooper, L. Balicas, N. E. Hussey, E. A. Yelland, S. Lee, A. Yamamoto, S. Tajima, S. M. Kazakov, et al., Phys. Rev. Lett. **91**, 37003 (2003).
- ¹⁷ P. B. Allen and B. Mitrović, Solid State Physics **37**, 1 (1982).
- ¹⁸ G. E. Reuter and E. H. Sondheimer, Proc. Roy. Soc. (London) Series A **195**, 336 (1948).
- ¹⁹ R. G. Chambers, Proc. Roy. Soc. (London). Series A **215**, 481 (1952).
- ²⁰ A. B. Pippard, *Advances in Electronics and Electron Physics*, vol. 5 (Academic Press, 1954).
- ²¹ D. C. Mattis and J. Bardeen, Phys. Rev. **111**, 412 (1958).
- ²² P. B. Allen, Phys. Rev. B **3**, 305 (1971).
- ²³ B. Farnworth and T. Timusk, Phys. Rev. B **10**, 2799 (1974).
- ²⁴ B. Farnworth and T. Timusk, Phys. Rev. B **14**, 5119 (1976).
- ²⁵ P. Tomlinson and J. P. Carbotte, Canadian Journal of Physics **55**, 751 (1977).
- ²⁶ H. K. Leung, F. W. Kus, N. McKay, and J. P. Carbotte, Phys. Rev. B **16**, 4358 (1977).
- ²⁷ E. Schachinger, D. Neuber, and J. P. Carbotte, Phys. Rev. B **73**, 184507 (2006).
- ²⁸ J. R. Anderson and A. V. Gold, Phys. Rev. **139**, A1459 (1965).
- ²⁹ E. R. Cowley, Sol. State Comm. **15**, 587 (1974).
- ³⁰ N. W. Ashcroft and N. D. Mermin, *Solid State Physics* (Saunders College, 1976).
- ³¹ N. W. Ashcroft, J. Phys. C **1**, 232 (1968).
- ³² N. Bock and D. Coffey (unpublished).
- ³³ M. Tinkham, *Introduction to Superconductivity* (Robert E. Krieger Publishing Company, Florida, 1980).
- ³⁴ R. R. Joyce and P. L. Richards, Phys. Rev. Lett. **24**, 1007 (1970).
- ³⁵ S. B. Nam, Phys. Rev. **156**, 470,487 (1967).
- ³⁶ G. D. Mahan, *Many-Particle Physics* (Plenum Press, New York, 1990).

- ³⁷ D. N. Basov and T. Timusk, Rev. Mod. Phys. **77**, 721 (2005).
- ³⁸ E. G. Maksimov, O. V. Dolgov, and M. L. Kulic, Phys. Rev. B **72**, 212505 (2005).
- ³⁹ P. S. Riseborough, Phys. Rev. B **27**, 5775 (1983).

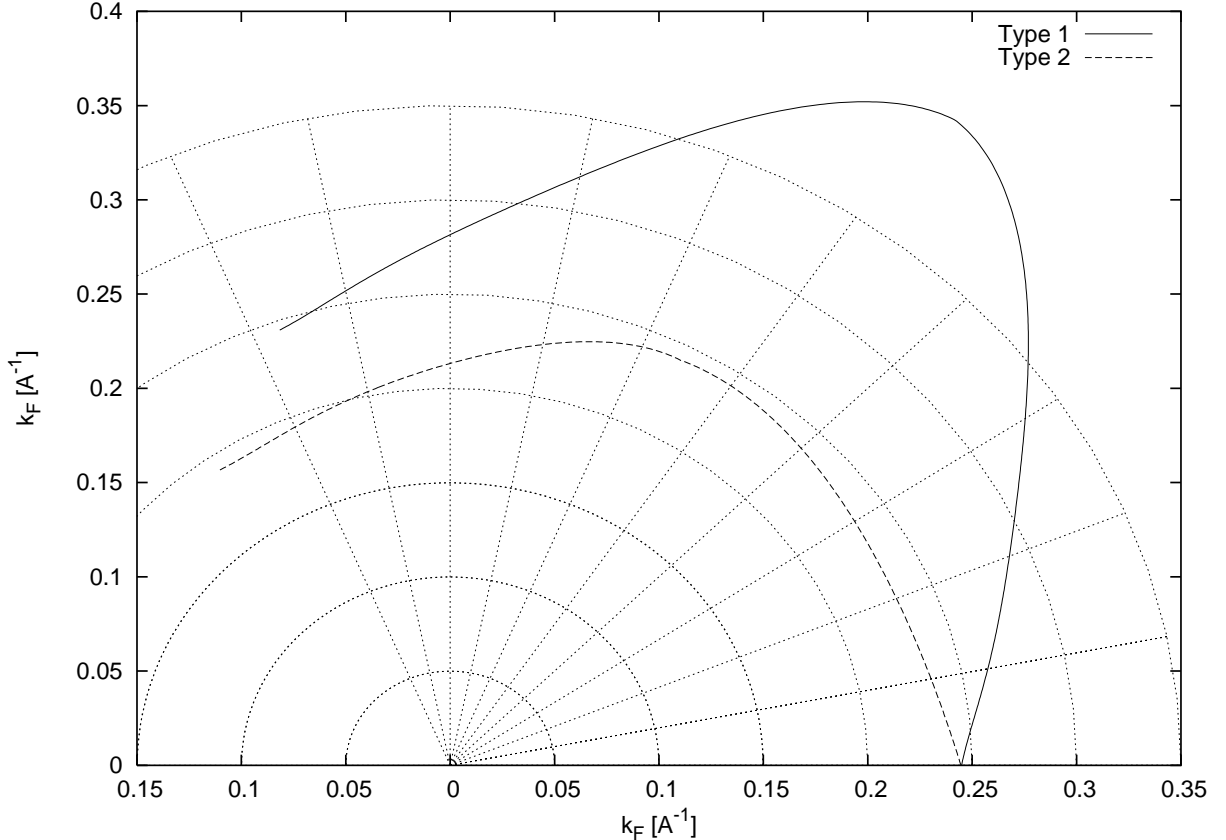


FIG. 12: The Fermi momentum as a function of angle β for the two types of third band pipes.

VII. APPENDIX: FERMI SURFACE PARAMETERIZATION

Although diagonalizing the Anderson and Gold 8x8 matrix is computationally not very challenging in itself, we will need to calculate its eigenvalues many times since we will integrate over the electron momentum. It turns out that using a diagonalization routine directly inside the integration is computationally not feasible. We therefore had to simplify the model.

As pointed out earlier, we will require two of the four bands only. The second band Fermi surface is close to spherical which led us to set the Fermi momentum in that band to a constant, $v_F^{(2)} = -1.367 \times 10^6 \text{ m s}^{-1}$. The second band is hole-like.

The third band Fermi surface consists of “pipes” which we approximated by dented cylinders. There are two types of pipes and we chose to parametrize these separately. In Fig. 12 we show the angular dependence of the Fermi momentum on each of the two pipes. The dispersion was linearized and the Fermi velocity we calculated for both types is $v_F^{(3)} = 1.055 \times 10^6 \text{ m s}^{-1}$. The third band is electron-like.